

This work was written as part of one of the author's official duties as an Employee of the United States Government and is therefore a work of the United States Government. In accordance with 17 U.S.C. 105, no copyright protection is available for such works under U.S. Law.

Public Domain Mark 1.0









<https://creativecommons.org/publicdomain/mark/1.0/>

Access to this work was provided by the University of Maryland, Baltimore County (UMBC) ScholarWorks@UMBC digital repository on the Maryland Shared Open Access (MD-SOAR) platform.

**Please provide feedback**

Please support the ScholarWorks@UMBC repository by emailing [scholarworks-group@umbc.edu](mailto:scholarworks-group@umbc.edu) and telling us what having access to this work means to you and why it's important to you. Thank you.

# Characterizing Thermal Background Events for *Athena* X-IFU

S. V. Hull , J. S. Adams, S. R. Bandler, S. Beaumont , J. A. Chervenak, R. Cumbee, F. M. Finkbeiner , J. Y. Ha, R. L. Kelley, C. A. Kilbourne , F. S. Porter , K. Sakai , S. J. Smith , N. A. Wakeham , E. J. Wassell, and S. H. Yoon

**Abstract**—The X-ray Integral Field Unit on *Athena* will be subject to a cosmic-ray induced thermal background on orbit, with energy depositions into the detector wafer leading to thermal bath fluctuations. Such fluctuations have the potential to degrade energy resolution performance of the transition-edge sensor based microcalorimeter. This problem was previously studied in simulations that modeled thermal bath fluctuations induced by cosmic-ray events and evaluated the resulting energy resolution degradation due to a simulated timeline of such events. Now taking an experimental approach, we present results using a collimated Am-241 alpha particle source to deposit a known energy to specific locations on the detector wafer. Thermal pulses induced by the alpha particle energy depositions are measured at various detector pixels for several different experimental configurations, including for energy deposited into the inter-pixel structure of the wafer, as well as the frame area outside the pixel array. Further, we also test both with and without a thick backside heatsinking metallization layer that is baselined for the instrument. In each case results are compared to expectations based on the thermal model developed for the previous study.

**Index Terms**—*Athena* space telescope, transition-edge sensor, cosmic-ray background, thermal background, detector heatsinking.

Manuscript received 18 November 2022; revised 1 March 2023; accepted 7 March 2023. Date of publication 14 March 2023; date of current version 27 March 2023. This work was supported by an appointment to the NASA Postdoctoral Program at the NASA Goddard Space Flight Center, administered by Oak Ridge Associated Universities under contract with NASA, and also based upon work supported by NASA under Grant 80GSFC21M0002. (Corresponding author: S. V. Hull.)

S. V. Hull, S. R. Bandler, J. A. Chervenak, R. L. Kelley, C. A. Kilbourne, F. S. Porter, S. J. Smith, and E. J. Wassell are with the NASA Goddard Space Flight Center (GSFC), Greenbelt, MD 20771 USA (e-mail: samuel.v.hull@nasa.gov).

J. S. Adams, K. Sakai, and N. A. Wakeham are with the Center for Space Sciences and Technology, University of Maryland, Baltimore, MD 21250 USA, and also with the NASA GSFC, Greenbelt, MD 20771 USA.

S. Beaumont is with the Center for Space Sciences and Technology, University of Maryland, Baltimore, MD 21250 USA, and with the IRAP, 31400 Toulouse, France, and also with the NASA GSFC, Greenbelt, MD 20771 USA.

R. Cumbee is with the University of Maryland, College Park, MD 20742 USA, and also with the NASA GSFC, Greenbelt, MD 20771 USA.

F. M. Finkbeiner is with the Sigma Space Corp./Hexagon US Federal, Lanham, MD 20706 USA, and also with the NASA GSFC, Greenbelt, MD 20771 USA.

J. Y. Ha is with the SB Microsystems, Glen Burnie, MD 21061 USA, and also with the NASA GSFC, Greenbelt, MD 20771 USA.

S. H. Yoon is with the Science Systems and Applications, Inc. (SSAI), Lanham, MD 20706 USA.

Color versions of one or more figures in this article are available at <https://doi.org/10.1109/TASC.2023.3257131>.

Digital Object Identifier 10.1109/TASC.2023.3257131

## I. INTRODUCTION

**A**BOARD the *Athena* X-ray Observatory — a large-scale astrophysics mission planned to launch in the 2030 s — the X-ray Integral Field Unit (X-IFU) will utilize a large, transition-edge sensor (TES) based microcalorimeter array to explore the “Hot and Energetic” X-ray Universe with exceptional spectral resolution of 2.5 eV [1]. In order to achieve this performance, the focal plane assembly (FPA) of X-IFU will need to withstand the thermal background that is created due to high energy cosmic rays (CRs) bombarding the satellite [2]. CRs and secondary particles that pass through the instrument structure will regularly deposit energy into elements of the FPA [3]; those events that deposit energy directly into TES pixels will contribute to the non-thermal instrument background, but will largely be rejected by the included cryogenic anti-coincidence detector [4]. However, CR events will also often deposit energy into the FPA detector wafer, thereby creating thermal-bath temperature ( $T_b$ ) fluctuations that have the potential to degrade instrument energy resolution ( $\Delta E$ ) — as has been observed to some degree in previous X-ray calorimeter instruments like *Suzaku* XRS [5] and *Hitomi* SXS [6].

The X-IFU detector wafer is a  $\sim 61 \text{ mm}^2$  hexagon that consists of a  $300 \text{ }\mu\text{m}$  thick Si substrate, a  $0.5 \text{ }\mu\text{m}$  thick, low-stress SiN membrane, and, in the central  $3 \text{ mm}^2$  of the wafer, a  $\sim 2000\text{--}3000$  pixel hexagonal detector array. Each pixel has a Mo/Au bilayer — the TES sensing element — and a Bi/Au X-ray absorber attached to the TES [7]. Each pixel is also back etched all the way to the SiN membrane, leaving the TES suspended on this membrane and therefore forming a weak thermal link to the bath. The back etch leaves a grid-like structure of Si beams between each pixel, which we call the *muntins*. The Si detector wafer can therefore be seen to have two main sections, the central muntin structure between TES pixels, as well as the continuous outer frame outside the array. For heatsinking purposes, a backside metallization coating is applied to the wafer, including both the muntins and outer frame, and a number of Au wirebonds are used to link the coating to the FPA cold head. Fig. 1 shows a photo of a prototype X-IFU detector wafer, while Fig. 2 shows a diagram of a TES pixel within the muntin structure.

To account for potential thermal background performance degradation, a model was developed to study the risks posed for X-IFU, and how well they might be mitigated through various

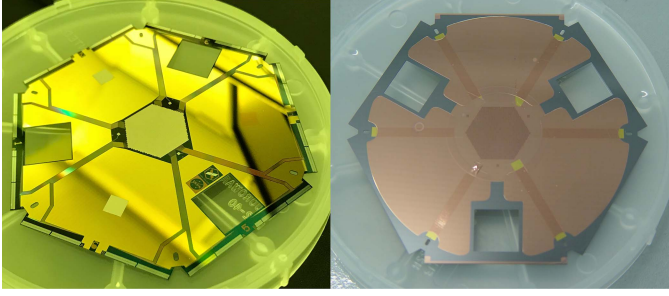


Fig. 1. Left: Photo of a 90 mm, prototype X-IFU detector wafer with  $\sim 3000$  TES pixels. 960 pixels are wired to the edge of the array, of which only a small subset ( $\leq 5\%$ ) are utilized for this work. Right: The prototype wafer seen from the reverse side, after deposition of  $3.5\ \mu\text{m}$  Cu heatsinking layer. Au backside metallization is baselined for X-IFU, but Cu has very similar thermal properties for heatsinking purposes and was used in this experiment.

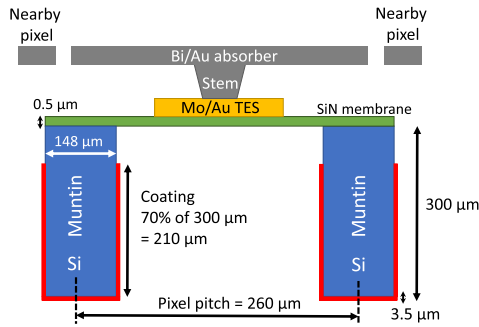


Fig. 2. Schematic of a single TES pixel, showing the Si beam (muntin) structure between pixels. A metallic coating is applied to the backside Si for additional heatsinking.

heatsinking schemes [8], [9]. A Geant4 simulation provided inputs to the model in the form of the expected count rate and spectrum for energy depositions into the wafer frame and muntins via CR events — predicting  $2\text{--}4\ \text{counts s}^{-1}\ \text{cm}^{-2}$  with an average deposited energy of  $\sim 450\ \text{keV}$  in the frame and  $\sim 250\ \text{keV}$  in the muntins. In addition, a finite-element method (FEM) model was developed using COMSOL Multiphysics to estimate the thermal pulses that will be induced in the wafer for a given energy and deposition location — and given the basic wafer and heatsinking geometries and the associated heat capacities and thermal conductances. More details on this FEM model can be found in [9]. Finally, the X-IFU end-to-end simulator was used to combine these inputs to model the TES response for a timeline of local  $T_b$  pulses at a given pixel. The effect of an individual CR-induced  $T_b$  pulse on a measured X-ray event is an offset on the measured energy. The end-to-end simulator evaluates the energy offset for each simulated CR event, building a histogram of energy offsets due to this thermal background signal, and thereby estimates the expected energy resolution degradation using the width of this distribution.

The modeling study used a baseline heatsinking configuration of  $3.5\ \mu\text{m}$  thick Au backside metallization coating, with  $\geq 500$  Au heatsinking wirebonds placed at the inner-most accessible locations on the wafer as determined by the design of the FPA wafer mount. Using this configuration, the expected  $\Delta E$  degradation (FWHM) was found to be  $0.02\ \text{eV}$  for muntin CR

hits, and  $0.06\ \text{eV}$  for outer frame CR hits (both for worst case pixels). The degradation is smaller for the muntin hits because of a lower count rate and smaller average deposition energy compared to the outer frame. These values are well below the  $0.2\ \text{eV}$  that has been allocated to thermal background in the X-IFU  $\Delta E$  error budget.

These modeling results suggest a minimal impact on X-IFU performance; however, there are still uncertainties for which increased confidence is desired — in particular the FEM thermal model with its inherent complexities. We now further explore thermal background events using an experimental approach. Here we attempt FEM model verification, hoping to provide additional evidence that the X-IFU heatsinking design will meet the aforementioned error budget allocation. We conducted this experiment using a prototype X-IFU wafer in order to fulfill one of the milestones needed to demonstrate a Technology Readiness Level<sup>1</sup> of 5 for the X-IFU FPA.

The experiment used an Am-241 alpha particle source to deposit energy directly into the prototype wafer at low count rates ( $< 1\ \text{counts/s}$ ), thereby simulating individual CR energy depositions. With this approach we do not attempt to simulate the in-flight CR environment, but instead to measure the effects of single energy depositions into the wafer while understanding their relation to modeling expectations. A similar approach to study the thermal background effects of CRs has been used in the past for *Suzaku* XRS [10], while other studies have also observed the effects of individual energetic particle depositions into a TES detector wafer [11]. In the remainder of this work, we present results of our testing along with a comparison to corresponding modeling results.

## II. EXPERIMENTAL SETUP

A collimated,  $0.9\ \mu\text{Ci}$  Am-241 alpha particle source was used to simulate the effects of CRs on the detector wafer and study heatsinking performance. The  $\sim 5.5\ \text{MeV}$  alpha particles emitted by the source were directed to specific points on the detector wafer using a mask, which was mounted to the backside of the detector assembly. Alpha particles absorbed in the wafer create wafer-scale thermal fluctuations, which are propagated to TES pixels and observed as signal pulses. Several different experimental configurations were tested. This includes both focusing of the alpha particles to the outer frame as well as to an individual muntin in the inter-pixel beam structure.

Two different masks were used in the experiment depending on the particular configuration: an etched Si mask with a  $100\ \mu\text{m} \times 100\ \mu\text{m}$  hole, and a machined Cu mask with a  $\sim 1\ \text{mm}$  diameter hole. The Si mask with the smaller hole was used to target alpha particle to a muntin, while the Cu mask was used for outer frame hits.

The detector wafer itself was kinematically mounted to the front side of a detector mount that sits at the head of a  $55\ \text{mK}$  cold stage. This wafer is an X-IFU prototype that shares both the basic functionality and approximate physical configuration

<sup>1</sup>[https://www.nasa.gov/pdf/458490main\\_TRL\\_Definitions.pdf](https://www.nasa.gov/pdf/458490main_TRL_Definitions.pdf)

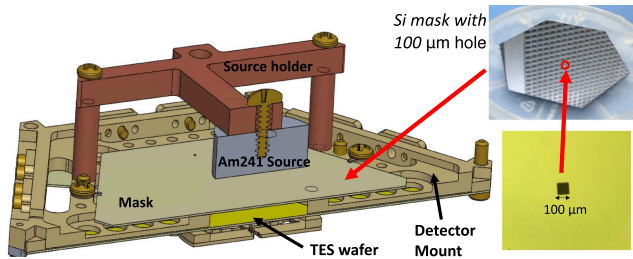


Fig. 3. Backside cutaway view of the alpha experiment mounting setup. The mask and Am-241 source are both secured to the reverse side of the detector mount as shown here. The Si mask with a  $100\ \mu\text{m}$  hole is pictured, but a Cu mask with larger  $1\ \text{mm}$  hole was also used for some configurations.

of the flight model, but with fewer wired pixels. While over three thousand TES pixels have been fabricated, only 960 pixels are wired to the edge of the wafer, and further only a small subsection of  $\sim 200$  pixels are connected for readout during this testing. On the order of 100 Au wire bonds ( $\sim 75\ \mu\text{m}$  thick wires using ball bonding) were distributed around the edge of the wafer for heatsinking the wafer to the mount; modeling shows that this configuration is expected to perform similarly to the flight-baselined 500 Au bonds.

Meanwhile, the mask was mounted to the reverse side of this detector mount using small clips, and a machined source holder mounted the Am-241 source behind the array. Fig. 3 shows a cutaway view of the experimental setup in CAD, viewed from the backside of the detector mount.

Initially, the Am-241 source was mounted roughly  $1\ \text{cm}$  away from the backside of the detector wafer as shown in Fig. 3; however, early testing in this configuration revealed that a very high residual magnetic ( $B$ ) field was being generated from magnetized materials in the stainless steel source housing. This field rendered the TES pixels completely inoperable as they could not be placed into the superconducting transition. The source was subsequently mounted approximately  $4\times$  further away to reduce field strength at the detector. This successfully allowed us to operate TES pixels, but still left a considerable residual  $B$ -field which could not be fully canceled by the in-situ, nulling-field coil. As a result, a non-spatially uniform residual  $B$ -field was present during testing, leading to spatial variation in TES response.

We made use of a Fe-55 X-ray source emitting Mn- $K\alpha$  X-rays at  $5.9\ \text{keV}$  to serve as a per-pixel calibration of alpha pulse signal amplitude. This per-pixel calibration accounts for non-uniformities in TES response, including those caused by the residual  $B$ -field. Data was collected in single-pixel readout mode. Pulses from alpha particle energy depositions were measured at TES pixels and compared to modeled alpha pulses, which are calculated by numerically solving the coupled TES differential equations for a change in  $T_b$  as provided by the FEM thermal model. When solving the TES differential equations, pixel parameters were adjusted so that simulated X-ray pulses approximately aligned with the measured X-ray pulse shapes for a given pixel — including both X-ray pulse height and fall time.

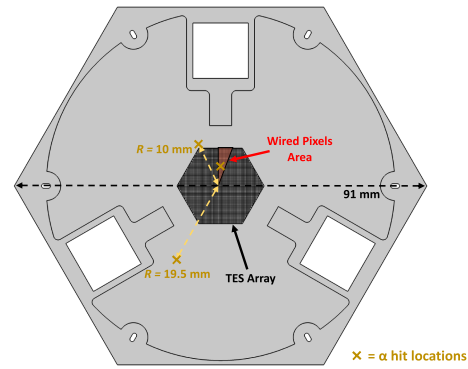


Fig. 4. Diagram of the wafer geometry used in the alpha particle experiment, showing the locations of alpha particle hits that were tested for different configurations, as well as the area of pixels that were fully wired for readout during the experiment. Results for the two locations in the frame at  $R = 19.5\ \text{mm}$  and  $R = 10\ \text{mm}$  are described in Sections III-A and III-B, while the location inside the array is described in Section III-C.

### III. RESULTS

#### A. Without Backside Heatsinking

Initial testing was completed without a thick backside heatsinking metallization layer in order to obtain the baseline response to alpha particle energy depositions. For these tests, the prototype wafer had a thin,  $0.5\ \mu\text{m}$ , layer of Au heatsinking on the front side, as is visible in the left photo of Fig. 1.

With this heatsinking configuration, the Am-241 source was separately tested while focused to two different locations on the outer frame:  $R = 19.5\ \text{mm}$  and  $R = 10\ \text{mm}$  ( $R \equiv$  radial distance from center of wafer to alpha particle hit). With a total wafer radius of  $45\ \text{mm}$  and TES array radius of  $9.5\ \text{mm}$ , this corresponds to points that are roughly in the middle of the outer frame, and just outside the TES array — see Fig. 4. For each test, several spatially dispersed pixels were tested to give a sense of spatial variation for alpha pulses. Altogether in both configurations, we tested pixels ranging from  $d = 6.1\ \text{mm}$  to  $d = 26.9\ \text{mm}$  ( $d \equiv$  distance from alpha particle hit to measured pixel).

We use the pulse height amplitude (PHA) measured at TES pixels as the primary figure of interest; for the remainder of the work this value is expressed as a percentage of the Mn- $K\alpha$  PHA to account for inter-pixel response variation. Here we find that the thermal pulses arising from energy depositions without heatsinking are quite small for all pixels ( $\text{PHA} \leq 1\%$ ), and, for measurements carried out at  $R = 19.5\ \text{mm}$ , difficult to detect over the noise background. In particular, the alpha PHA ranges from  $0.13\%$  at  $d = 26.9\ \text{mm}$ , to  $0.77\%$  at  $d = 6.1\ \text{mm}$ . See Fig. 5 for example average alpha pulses compared to Mn X-ray data.

When compared to pulses derived from the FEM model, the measured PHAs in these configurations are significantly smaller, by factors of up to  $\sim 5$  times. Focusing on the  $R = 10\ \text{mm}$  configuration, Fig. 6 compares measured average alpha pulses to modeled pulses for two spatially separated pixels. We find that for the central pixel furthest from the alpha-hit the model over-predicts the result by a factor of  $4.8$ , while for the edge

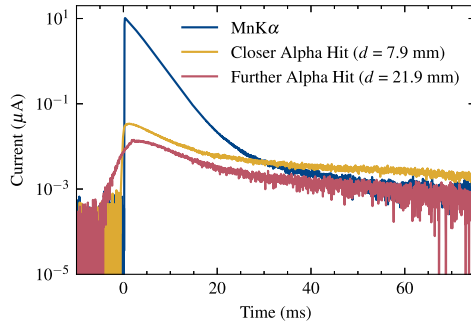


Fig. 5. Average alpha pulses measured at the same TES pixel and compared to MnK $\alpha$  pulse, for two different experimental configurations:  $R = 19.5$  mm and  $R = 10$  mm. The alpha PHAs are 0.19% and 0.33% of the MnK $\alpha$  PH respectively. The values for  $d$  denote the distance between the alpha hit the measured pixel in each configuration.

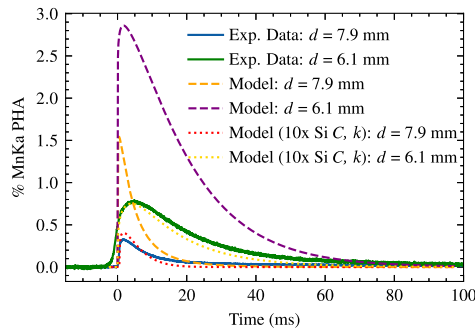


Fig. 6. Average alpha pulses measured as two spatially separated TES pixels in the  $R = 10$  mm configuration without backside heatsinking. Measurements are compared to pulses derived from both the baseline FEM model, as well as to the model adjusted with a factor of 10 applied to the Si heat capacity and conductivity.

pixel closest to the alpha-hit the model over-predicts the result by a factor 3.7. Similar levels of model over-prediction are seen for other pixels, including in the  $R = 19.5$  mm configuration.

The model can reproduce pulses much closer to measurements if the Debye heat capacity ( $C_v$ ) of the Si wafer is increased from the baseline model value, with a corresponding increase in the Si thermal conductivity as well. The model assumes a simple diffusive phonon thermal conductivity in Si as given by  $k = \frac{1}{3} C_v \nu_p \lambda_p$  ( $\nu_p \equiv$  phonon velocity;  $\lambda_p \equiv$  phonon mean free path), so naively increasing  $C_v$  also increases  $k$  by the same amount. In particular, an order-of-magnitude increase in  $C_v$  (and therefore also  $k$ ) was seen to result in model-derived pulses matching much closer to experimental data — see Fig. 6.

In previous thermal background experiments it has been observed that excess Si heat capacity at the approximate order-of-magnitude level is needed to match observed pulses; for example, in a similar alpha particle experiment carried out on a *Suzaku* XRS test array, a 20x factor applied to Si  $C_v$  was needed to match measurements [10]. This excess heat capacity could be related to the presence of surface oxides and/or fabrication-related films on the wafer. In addition, preliminary model validation of the X-IFU model adapted for *Hitomi* data also found it necessary to increase Si  $C_v$  and  $k$  by an order of magnitude. The increased thermal conductivity likely implies the simple diffusive model being

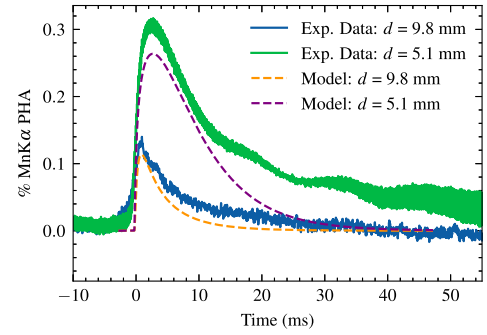


Fig. 7. Average alpha pulses measured as two spatially separated TES pixels, for a frame event at  $R = 10$  mm after deposition of  $3.5 \mu\text{m}$  Cu for backside heatsinking. The pulse data is compared to modeled pulses derived from the baseline FEM model, to which it closely aligns.

used is inadequate to accurately capture phonon heat transport in the Si and other physics, such as ballistic transport, needs to be added.

### B. With Backside Heatsinking

After completing the baseline testing described above, a heatsinking metallization layer is applied to the prototype wafer. While Au heatsinking is baselined for X-IFU, we use Cu for reasons of ease and cost, and because it has similar thermal properties to Au. Approximately  $3.5 \mu\text{m}$  of Cu is applied to the backside of the wafer, as shown in right of Fig. 1. Two different masks were used in the deposition that allowed the inner frame to be treated separately. In the inner muntin area, angled deposition was used to deposit Cu on the sides of the Si muntins; we estimate that Cu was deposited down roughly 70% of the well depth. The thickness of the Cu on the side walls is estimated to range from 0– $1.5 \mu\text{m}$ , with the thickness decreasing moving further down the wells.

Due to previously observing very small pulses that were difficult to measure in the  $R = 19.5$  mm setup without backside heatsinking, we tested only at  $R = 10$  mm here. In this configuration, we observe alpha PHAs ranging from 0.12% – 0.31% ( $d = 9.8$  mm to 5.1 mm), accounting for roughly a 50% reduction compared to the same configuration without backside heatsinking.

These measurements closely match expectations from the baseline FEM model, as shown in Fig. 7, where the measured PHAs can be seen to be within  $\sim 10\%$  of the modeled PHAs for both a central and edge pixel — despite the fact that baseline testing presented in Section III-A found pulses significantly smaller than expectations. This is because the thermal characteristics of the detector wafer become dominated by the thick backside Cu, and are minimally impacted by the Si wafer properties; adding a factor of 10 to the Si heat capacity and/or conductivity has little-to-no effect on model predictions for frame hits more than a few mm outside the array. Therefore, the baseline model can be seen to relatively accurately predict pulses in the frame — solidifying findings that the baseline heatsinking configuration is sufficient for frame events.

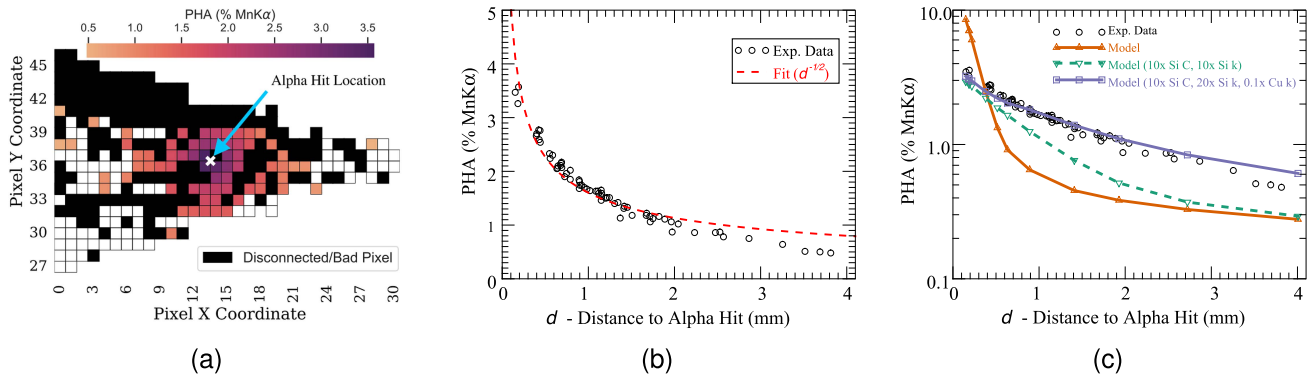


Fig. 8. (a) Alpha pulse-height amplitude (PHA) heatmap, showing a spatial map of the pixels used in the muntin-hit configuration. This map shows only those pixels potentially available for readout, which is a small subsection of the full TES array. The pixels that are shaded black were not fully connected for readout or were otherwise unusable. The color shading shows the PHA from alpha energy depositions at the marked location, while the pixels in white were untested. (b) Plot of alpha PHA vs. distance from alpha energy deposition in the muntin. A  $d^{-1/2}$  fit is also shown, to demonstrate the relative slowness of PHA decay with distance. (c) The same data shown in (b), but with several FEM model results overlaid for comparison. The baseline model has significant departures from the data, while closer agreement can be obtained with some parameter variation, which is likely not physical in all cases — see text for discussion.

### C. Muntin Hits

Finally, we use an experimental setup that deposits energy from alpha events directly into the inter-pixel muntin structure of the wafer. In this case we tested solely in a configuration with thick backside heatsinking, primarily due to preliminary simulations showing that the alpha signal would be overwhelming in nearby pixels without backside heatsinking.

The Si mask is roughly aligned to the array area of connected pixels and experimental PHA data is used to confirm exact spatial positioning, as precise manual alignment was found to be impossible for the  $100\ \mu\text{m}$  hole. With a strong spatial PHA gradient for this test, we measure a large number of pixels in the surrounding area — the results of which are summarized in Fig. 8. The pixels directly adjacent to the alpha energy deposition are measured with a PHA of  $\sim 3.5\%$ , while the PHA decreases as distance is increased, and falls below  $1\%$  at a distance of roughly  $2\ \text{mm}$ . The spatial positioning of the alpha hit (to derive these distances) was calculated as the 2D centroid of the measured alpha PHA data. A full spatial PHA heatmap is displayed in Fig. 8(a), while Fig. 8(b) shows the same PHA data plotted as a function of distance to the alpha energy deposition — also showing a  $d^{-1/2}$  fit for comparison.

There are significant differences between the model predictions and these experimental results. This is shown in Fig. 8(c), which plots the same experimental data, but also compares it to FEM-model-derived results. We see that the model predicts a much larger initial pulse in the first  $0.5\ \text{mm}$  ( $\sim 6\%–8\%$ ), followed by a rapid decline to less than  $1\%$ , meaning that the model under-predicts experimental data (by roughly  $50\%$ ) for all but the closest pixels.

Within the first few mm of the alpha energy deposition, model results with backside heatsinking are fairly sensitive to the Si properties — unlike in the case of further away frame hits — and, in general, to any parameter variation. Adjusting the Si properties as was found to be needed in Section III-A ( $10\times$  heat capacity and, as a result, also thermal conductivity) improves model–data agreement to an extent, shown in Fig. 8(c). As

explained in the above section, this increased Si heat capacity is not particularly surprising and has been observed in similar previous experiments.

However, even after increasing the Si heat capacity, significant differences between the data and model remain. Much closer convergence can be achieved by also reducing the electronic thermal conductivity of the backside Cu by a factor of 10 and further increasing the Si conductivity by another factor of 2 (again see Fig. 8(c)). However, we note that this is neither a perfect match nor a necessarily unique solution — only the best result achieved with a simple, coarse parameter variation analysis.

Despite better agreement with data, there is no clear justification for reducing the Cu electronic thermal conductivity. The baseline value used in the model is calculated using the Wiedemann-Franz-Lorenz law, using a measured RRR value, and therefore is thought to be generally accurate. As mentioned above, it is possible another model variation better describes the data. Alternatively, the apparent need to reduce Cu thermal conductivity may only be a symptom of general limitations of the model physics and/or geometry. The temperature change implied by the model for the closest pixels is up to  $\sim 0.5\ \text{K}$  — a quite large variation to cover with the model physics. It may also be that the geometries for the muntin structure and its backside heatsinking are not being well-captured by the somewhat simplified model representations.

## IV. CONCLUSION

We performed an experiment using an Am-241 alpha particle source to simulate individual energy deposition from CRs into a prototype X-IFU detector wafer, testing different deposition locations and heatsinking configurations. Measuring the signal from alpha depositions with TES array pixels, we compare results to predictions using a FEM model.

Without backside heatsinking, the baseline model significantly over-predicts the expected alpha pulses until increasing the Si heat capacity and thermal conductivity by an order of

magnitude — a result aligning with previous findings. With backside heatsinking, the model accurately predicts alpha particle pulses for outer frame depositions; however, for muntin hits the model over-predicts the pulse height within the first 0.5 mm before beginning to under-predict at further distances. The disparity is reduced but not fully eliminated with the aforementioned adjustment for Si properties, suggesting additional complexity not currently being accounted for in the model.

Despite somewhat uneven model performance, these findings do support a minimal level of impact on X-IFU from CR-induced thermal background with baselined heatsinking. In most situations the model either accurately predicts or over-predicts the pulses from energy depositions, only somewhat under-predicting for muntin hits at the intermediate distances. Meanwhile, previous work using this model to evaluate the impact on X-IFU has shown there is significant margin to meet the X-IFU  $\Delta E$  error budget requirements, particularly in the muntin hit case. Furthermore, the  $\Delta E$  degradation for muntin hits is most strongly dependent on the largest amplitude pulses (i.e. from nearest neighbor pixels), which appear smaller than expected. Given these findings, the baseline heatsinking configuration should allow for minimal degradation to instrumental performance due to cosmic-ray events. Indeed, preliminary results from updated modeling to evaluate the performance impacts of the muntin hit model–experiment divergence are consistent with the same or lower  $\Delta E$  degradation compared to previous results. In the future we plan to continue studies of X-IFU's thermal background and perform a similar alpha experiment with a higher fidelity prototype flight wafer.

#### ACKNOWLEDGMENT

We would like to thank Antoine Miniussi for providing many useful discussions and inputs into the preparation of this work.

In addition, we would also like to thank Steve K. Brown for generously providing the Am-241 source used in this work.

#### REFERENCES

- [1] D. Barret et al., "The Athena X-ray Integral Field Unit: A consolidated design for the system requirement review of the preliminary definition phase," *Exp. Astron.*, pp. 1–54, 2023, doi: [10.1007/s10686-022-09880-7](https://doi.org/10.1007/s10686-022-09880-7).
- [2] S. Lotti et al., "Review of the particle background of the Athena X-IFU instrument," *Astrophysical J.*, vol. 909, no. 2, 2021, Art. no. 111.
- [3] S. Lotti et al., "Estimates for the background of the ATHENA X-IFU instrument: The cosmic rays contribution," *Proc. SPIE*, vol. 10699, 2018 Art. no. 106991Q, doi: [10.1117/12.2313236](https://doi.org/10.1117/12.2313236).
- [4] C. Macculi et al., "The Cryogenic Anticoincidence Detector for Athena X-IFU: A program overview," *Proc. SPIE*, vol. 9905, 2016, pp. 819–832.
- [5] C. Kilbourne et al., "Analysis of the Suzaku/XRS background," *Nucl. Instrum. Methods Phys. Res. Sect. A: Accel., Spectrometers, Detect. Assoc. Equip.*, vol. 559, no. 2, pp. 620–622, 2006. [Online]. Available: <https://www.sciencedirect.com/science/article/pii/S0168900205025519>
- [6] C. A. Kilbourne et al., "In-flight calibration of Hitomi soft X-ray spectrometer. (1) Background," *Pub. Astronomical Soc. Jpn.*, vol. 70, no. 2, 2018, Art. no. 18, doi: [10.1093/pasj/psx139](https://doi.org/10.1093/pasj/psx139).
- [7] S. J. Smith et al., "Performance of a broad-band, high-resolution, transition-edge sensor spectrometer for X-ray astrophysics," *IEEE Trans. Appl. Supercond.*, vol. 31, no. 5, Aug. 2021, Art. no. 2100806.
- [8] P. Peille et al., "Quantifying the effect of cosmic ray showers on the X-IFU energy resolution," *J. Low Temp. Phys.*, vol. 199, no. 1, pp. 240–249, 2020, doi: [10.1007/s10909-019-02330-3](https://doi.org/10.1007/s10909-019-02330-3).
- [9] A. R. Miniussi et al., "Thermal impact of cosmic ray interaction with an X-ray microcalorimeter array," *J. Low Temp. Phys.*, vol. 199, no. 1, pp. 45–55, 2020, doi: [10.1007/s10909-020-02337-1](https://doi.org/10.1007/s10909-020-02337-1).
- [10] C. Stahle et al., "Cosmic ray effects in microcalorimeter arrays," *Nucl. Instrum. Methods Phys. Res. Sect. A: Accel., Spectrometers, Detect. Assoc. Equip.*, vol. 520, no. 1, pp. 472–474, 2004. [Online]. Available: <https://www.sciencedirect.com/science/article/pii/S0168900203032960>
- [11] R. Hayakawa et al., "Waveform analysis of a 240-pixel TES array for X-rays and charged particles using a function of triggering neighboring pixels," *J. Low Temp. Phys.*, vol. 200, no. 5, pp. 269–276, 2020, doi: [10.1007/s10909-020-02449-8](https://doi.org/10.1007/s10909-020-02449-8).